Construction of K+ ions gradient in crystalline carbon nitride to accelerate charge separation for efficient visible light H2 production

Guoqiang Zhang
Shenzhen University
Yangsen Xu
Shenzhen University https://orcid.org/0000-0002-0907-1601
Chuan-Xin He
Shenzhen University https://orcid.org/0000-0002-2254-360X
Yongliang Li
Shenzhen University https://orcid.org/0000-0002-5008-0868
Xiangzhong Ren
Shenzhen University
Peixin Zhang
Shenzhen University
Hongwei Mi (milia807@szu.edu.cn)
Shenzhen University https://orcid.org/0000-0002-4643-1768

Article

Keywords: crystalline carbon nitride, charge separation, gradient doping, built-in electric field, photocatalytic H2 generation

Posted Date: January 18th, 2021

DOI: https://doi.org/10.21203/rs.3.rs-145087/v1

Abstract

Like most of the recent reported semiconductor photocatalysts, the sluggish dynamic charges transfer and separation caused by weak driving force still restricts the further improvement of photocatalytic performance in crystalline carbon nitride (CCN). Here, we successfully prepared a series of heptazine-based K+ implanted CCN (KCN) for the first time, where the K+ ions concentration was gradiently inserted through controlling its diffusion from the surface to bulk in carbon nitride (CN). As a powerful driving force, the built-in electric field (BIEF) induced by this concentration gradient, greatly accelerates the drift movement and the transport from bulk to the surface, as well as the separation of photogenerated carriers. Consequently, the KCN with optimized BIEF displays a ~34 times promotion than original CN for visible-light H2 evolution. Such a high activity enhancement factor is at a relatively good level in reported CCN. Our proposed strategy to induce BIEF production by constructing concentration gradients through thermodynamically feasible diffusion controlled solid-state reaction, can be adopted to build other efficient photocatalytic systems.

1. Introduction

Polymer carbon nitride (CN) has attracted extensive attention due to its unique semiconductor band structure, excellent chemical stability, metal-free components, and easy preparation with cheap and plentiful readily available nitrogen-containing precursors.[1] However, due to the limited mobility of reaction intermediates, the traditional thermal polymerization of CN always faces the bottleneck of incomplete polymerization, resulting in its amorphous melon-based structure.[2,3] This amorphous structure leads to the formation of weakly conjugated aromatic ring system and the difficulty of charges transfer on the polymer plane. In recent years, crystalline carbon nitride (CCN) has been constructed by solid or molten salt assisted methods and emerged as a promising candidate to drive solar energy conversion.[4] On the one hand, the highly polymerized heptazine units in CCN can furnish an unimpeded charges transfer channel on the two-dimensional (2D) π-conjugated plane, which effectively accelerates the charges transfer and exciton dissociation of intralayer.[5] On the other hand, its shorter π-π stacking distance than amorphous melon-based CN, promotes charges transfer and excitons dissociation between layers. As a result, this advanced structure makes CCN much more active than amorphous CN.

Although much progress has been made in CCN, the bottleneck of charges transfer and separation similar to most photocatalysts still restricts the further improvement of its performance. The process of charges separation is closely related to the migration of photogenerated carriers in semiconductors.[6] According to the driving force of photogenerated carrier migration, it can be divided into diffusion motion and drift motion.[7,8] For photoelectrocatalysis, the carriers drift motion caused by applied electric field greatly improves the efficiency of charge transfer and separation, so the efficiency is much higher than that of photocatalysis. Unfortunately, in photocatalysis, the photogenerated non-equilibrium carriers migrate to the photocatalyst surface through diffusion motion to participate in the reaction. This weak driving force results in fairly low photogenerated carriers transfer and separation.[7,8]

Building built-in electric field (BIEF) is one of the effective strategies to enhance the transport and separation of photogenerated carriers.[9-12] As a powerful driving force, the BIEF can induce the electrons and holes transport in opposite directions, and accelerate the separation of photogenerated electron-hole pairs. Although the BIEF can be induced by constructing heterojunctions using semiconductors with matched energy levels, their junction interfaces may become traps and recombination centers for carriers, weakening or even canceling the effects of carriers transport and separation.[13] In addition, the formation of heterojunctions requires specific interface matching and atom-level contact, which makes them difficult to construct. Gradient doping can lead to gradient changes in the electronic structures, band positions and bandgap energy among the same semiconductor. Similar to heterojunctions, this difference can generate a BIEF.[13-15] Fortunately, the BIEF constructed by gradient doping can eliminate the influence of disadvantageous factors such as heterogeneous junction interface and obtain higher photogenerated carriers separation efficiency. In addition, this BIEF is distributed throughout the semiconductor, which can greatly improve the drifting motion of carriers and enable more carriers to be transmitted to the surface for photocatalytic reaction. Onishi'group proposed that the gradient distribution from Sr-rich surface to Sr-poor core is spontaneously generated by diffusion controlled solid-state reaction during the preparation of $NaTaO_3$ photocatalyst.[16] This induced BIEF drives the separation of excited electrons from complementary holes, thereby restricting recombination. Yu et al built a suitable band structure by gradient doping carbon-ring in CN structure.[13] The resulting BIEF pushes electrons and holes in different directions, which increases the photocatalytic activity by 21 times. Due to these positive effects, the BIEF induced by gradient doping is expected to further optimize CCN activity.

Herein, gradient doping in heptazine-based K^+ implanted CCN (KCN) was successfully realized for the first time, through controlling the diffusion of K^+ ions from the surface to bulk in CN. Such gradient doping makes the electronic structures, band positions and bandgap energy with gradient changes in different depth regions from the surface to bulk of KCN, and the induced BIEF greatly accelerates the drift movement, transmission and separation of photogenerated carriers. Consequently, the KCN with the largest BIEF intensity presents the highest H_2 production rate of 261.9 μmol/h and 557.2 μmol/h/m^2 under visible light, which are approximately 22- and 34- times better than original CN, respectively. In a word, this strategy of gradient doping through thermodynamically feasible diffusion, and thus inducing BIEF generation to accelerate photogenerated carriers separation, can be widely applied to the construction of other efficient photocatalytic systems.

2. Results And Discussion

2.1 Preparation process

As shown in Figure 1a, the amorphous CN is obtained by thermal polymerization of melamine at 550℃ in the air for 3 h. Subsequently, its amorphous structure can be recrystallized by using KCl as structure inducer to furnish K^+ implanted CCN.[17] Figures 1b-c shows the proposed structure of heptazine-based CN and KCN. The gap between one-dimensional amine-linked heptazine-based melon chains in CN provides

a very good diffusion channel for K^+ ions. In addition, the diameter of K^+ ions (0.276 nm) is smaller than the interlayer spacing of CN (0.32 nm), so its interlayer is also a feasible diffusion channel. It can be predicted that with the increase of diffusion time, the K^+ ions concentration gradient will gradually increase. When the heat treatment reaches a certain time, the surface and bulk concentration of K^+ ions tend to be uniform, and the gradient will decrease. Therefore, the K^+ ions gradient doping in KCN can be constructed by controlling the diffusion time. The structure of KCN consists of one-dimensional amine-linked heptazine-based melon chains, in which K^+ ions are inserted in the interstitial region.[18,19] The adjacent polymer chains are extended into 2D supramolecular arrays by hydrogen bonding. According to the different maintain time at 600℃, we denote the samples as KCN *x* (*x* = 0.5-4), where *x* is the maintain time. The yield of the prepared samples with the increase of KCl treatment time were shown in Figure S1. The quality of obtained KCN increased first and then decreased. This is because the initial K^+ ion embedding leads to the increase of sample mass. Then the thermal decomposition of the KCN causes the mass to begin to decrease. The thermogravimetry (TG, Figure S2) further confirmed our conjecture. All the samples showed similar thermal stability and began to decompose at about 600℃.

2.2 Structure characterization and *absorption properties*

Elemental analysis (Table S1) shows that the atomic molar ratio of C/N in CN is 0.653, which is close to that of melon (0.67). With the extension of treatment time by KCl, the molar ratio increased from 0.668 (KCN 0.5) to 0.688 (KCN 2) and 0.714 (KCN 4). At the same time, the content of K element in KCN samples boosted from 3.13% (KCN 0.5) to 10.80% (KCN 2) and 15.19% (KCN 4), as estimated by inductively coupled plasma (ICP, Table S2) analysis. These results confirmed a structure composed of heptazine-based melon framework with intercalated K^+ ions. The typical X-ray diffraction (XRD) patterns of CN and KCN *x* (*x* = 0.5-4) is shown in Figures 2a-b. The CN appears two typical diffraction peaks at 12.9° and 27.6° identified as the (1 0 0) and (0 0 2) facets, respectively. In sharp contrast to CN, the main peak of the (0 0 2) facet experienced a gradual shift from 27.6° to 28.2° with the increase of KCl treatment time, indicating the interlayer spacing narrowed from 0.323 to 0.316 nm owing to the intercalation of K^+ ions in heptazine-based melon framework. It should be emphasized that this interlayer spacing narrowing is beneficial to the transfer of photogenerated carriers between adjacent layers. The other two diffraction peaks at 8.0° and 9.9° belong to the (1 1 0) and (0 2 0) facets, respectively.[18,19] Besides, those three peaks gradually narrowed and sharpened, indicating the crystallinity has been significantly improved. The full width at half maxima (FWHM) of XRD can reflect the change of crystallinity to a certain extent. As shown in Table S3, the FWHM values narrowed, indicating that the crystallinity of KCN gradually elevated with the thermal treatment. Thus, the structure inducer of solid KCl could recrystallize the amorphous structure during thermal treatment with CN. The color of KCN samples gradually deepens with the increase of annealing time, which vividly indicates the narrowing of bandgap (Figure 2c). The ultraviolet-visible diffuse reflectance spectra (UV-Vis DRS, Figure 2d) demonstrates an obvious red-shift in the absorption edge as the intercalation of K^+ ions. The KCN 4 appears the widest absorption region up to 480 nm among all samples, while original CN shows an optical absorption edge at 460 nm. In addition, the bandgap shows about 0.11 eV narrowing from 2.77 eV (CN) to 2.66 eV (KCN

4) observed in Tauc plots (Figure 2e). This narrowing of the bandgap may be due to the expansion of conjugated structure caused by the enhancement of crystallinity.

The characteristic structure was analysed via Fourier Transform Infrared Spectroscopy (FTIR, Figure 3a) to explore the structure-induced effect of KCl during thermal treatment with CN. The fingerprint signals at 1200-1700 cm^{-1} attribute to the stretching and bending vibration of conjugated CN heterocycles, while the peak at 810 cm^{-1} is the out-of-plane bending of the heptazine rings.[20,21] The typical C-N vibration signal emerges at 993 and 917 cm^{-1}, and the new peak at 1156 cm^{-1} can be attributed to the N-H bending vibration. In addition, KCN presents a new peak at 2180 cm^{-1} ascribed to the stretching modes of cyano group (C≡N), which probably results from the decomposition or incomplete polymerization of heptazine units.[18,22] X-ray photoelectron spectroscopy (XPS) was used to characterize the chemical bindings on the sample surfaces. As shown in XPS survey spectra (Figure S3), it confirmed the presence of C, N, O, K and Cl elements in KCN, while only C, N and O elements existed in CN. The residual Cl content in KCN is estimated to be 0.2 wt% (Figure S4). The C 1s spectrum presents three contributions, located at 288.1, 286.4 and 284.8 eV, respectively (Figure 3b). The two peaks around 288.1 and 284.8 eV in KCN are similar to CN, which can be attributed to C atoms in aromatic N-C=N units and graphitic carbon, respectively.[3,23] The weak peak in the middle at 286.4 eV originates from C≡N species, consistent with the FTIR analysis.[24] As shown in Table S4, the ratio of C≡N in C 1s XPS spectra (Figure 3b) ranges from trace (CN) to 0.07 (KCN 2) and 0.09 (KCN 4). In addition, compared with CN, the proportion of graphite carbon increases remarkably after the intercalation of K^+ ions in heptazine-based melon framework, which may be due to the improvement of crystallinity and conjugation. In N 1s XPS spectra (Figure 3c), both CN and KCN present three similar binding energy peaks. The peaks at 398.4 and 399.9 eV could be classified as the N atoms of C-N=C and N-$(C)_3$ in heptazine units.[3] Other peaks at 400.8 eV belongs to the N atoms in bridging -NH_x or C≡N species. Furthermore, the possible chemical structures were characterized by ^{13}C cross-polarization (CP)-MAS solid-state NMR spectrum (Figure 3d). The two distinct resonance bands at 156.8-157.4 ppm and 163.8-165.3 ppm can be attributed to the C atoms in the C-N_3 and CN_2-(NH_x) groups,[25-27] further confirming the existence of heptazine frameworks in CN and KCN. The peak at 168.5 ppm could be assigned to the C atom near the electron-withdrawing group (-C≡N) in KCN.

2.3 Morphology characterization

The field emission scanning electron microscope (FE-SEM) and transmission electron microscopy (TEM) images shows that the as-prepared KCN 2 sample consists of nanoparticles roughly 100-500 nm in diameters (Figures 4a-c), while CN presents the typical amorphous structure of polymer (Figure S5). No lattice fringes can be observed in high-resolution TEM (HR-TEM) image (Inset in Figure S5d) of CN. Contrarily, KCN 2 sample has good crystallinity with obvious lattice fringes and a (1 1 0) interlayer spacing of 1.102 nm (Inset in Figure 4c), further explained that the crystallinity has been greatly improved after the intercalation of K^+ ions in heptazine-based melon framework. The nanoparticles were also analysed using Scanning TEM (STEM) coupled with energy dispersive X-ray spectroscopy (EDX) to investigate the elements distribution. The high-angle annular dark-field STEM (HAADF-STEM) image in

Figure 4d appears a clear outline of the nanoparticles. The corresponding distribution of C, N, O and K elements is relatively uniform in the whole area (Figures 4e-h). An EDX line from a single nanoparticle from the images in Figures 4i-j is highlighted by a green line, with the elements distribution of the cross section displayed in Figures 4k-l. In a given area of both KCN 2 and KCN 4 samples, the elements content of C and N is relatively homogeneous. Interestingly, the distribution of K element in the two samples is quite different. The distribution of K element in KCN 4 is basically the same in the corresponding region, while its count in KCN 2 gradually decreases from the surface to the centre. This directly indicates that in the process of KCl thermal treatment, a gradient of K^+ ions can be formed due to its diffusion from the surface to the bulk. Finally, its concentration on the surface and in the bulk tends to be uniform with the increase of diffusion time. The Brunauer-Emmett-Teller (BET) surface area and pore size distribution are measured by using N_2 adsorption-desorption isotherm (Figure S6). With the intercalation of K^+ ions in heptazine-based melon framework, the BET surface areas show a slight decrease, which are measured to be 14.5, 13.3, 9.4 and 9.0 m^2/g for CN, KCN 0.5, KCN 2 and KCN 4, respectively. The pore size distribution curves present the typical macroporous structure originated from the accumulation of nanoparticles.

2.4 Characterization of K^+ ion concentration gradient and BIEF

XPS with different depth etched by argon ion was used to further verify the concentration gradient of K^+ ions (Figures 5a-b). Two binding energy around 292.9 and 295.7 eV are attributed to K^+ ion,[28] which is different from that of metal K (294.7 eV). In addition, the doublet separation of K 2p photoelectron lines is 2.8 eV, which further confirms the presence of K^+ ion. With the depth of Ar ion etching from 0 to 100 nm, the strength of K^+ ions decreases gradually, and the atomic ratio of K reduces sharply from 13.24% to 4.32%, indicating the existence of K^+ ion gradient in KCN 2. Contrarily, in KCN 4 sample, the atomic ratio of K does not change significantly from 14.18% to 11.93% with the increase of etching depth (0-100 nm). This is due to the increase of diffusion time of K^+ ions, and its concentration in surface and bulk tends to be relatively uniform. In addition, the etched valence band XPS (VB-XPS) spectra at different depths are used to investigate the changes of VB positions at different depths. As shown in Figures 5c-d, the VB position in KCN 2 and KCN 4 are located at 2.70 eV below Fermi level. With the increase of etching depth, the VB position moves upward gradually. From the surface to 100 nm, the VB position of KCN 2 presents a shift of 0.28 eV, while that of KCN 4 is only 0.12 eV. This difference of VB position between surface and bulk phase, caused by the concentration gradient of K^+ ions, is beneficial to generate a BIEF, which promotes the separation of photogenerated carriers and the transport from bulk to the surface.

The intensity of BIEF for KCN samples was estimated using the model established by Kanata,[10,11] which indicates that the BIEF strength is determined by the surface potential and surface charge density. Firstly, the surface potential was measured using the Atomic Force Microscopy (AFM) at the surface potential mode (Figures 6a-d). Their two-dimensional field is significantly different among all KCN samples, but relatively uniform for each sample. The surface potential was determined to be 624.7, 1025.2 and 769.8 mV, respectively. Secondly, we measured the Zeta potential of KCN samples in triethanolamine (TEOA) solution. The trend of these results is consistent with the changes of surface potential, which is

determined to be -22.7, -32.5 and -29.8 mV (Figure 6e). Subsequently, the surface charge density was calculated using the measured Zeta potential and Gouy-Chapman model.[29] Because the surface charge density is determined by the Zeta potential,[30] the BIEF of KCN samples can be estimated by surface potential and Zeta potential. Finally, the BIEF strength of KCN 2 and KCN 4 samples is 2.4 and 1.6 times higher than that of KCN 0.5 (Figure 6f). These characterizations demonstrate the existence of BIEF in KCN samples induced by the concentration gradient of K^+ ions.

2.5 Testing and interpretation of photocatalytic activity

The enhanced crystallinity and successfully constructed BIEF help to explore their photocatalytic activity under visible light. The 50 mg of samples added with H_2PtCl_6 (3 wt% Pt) is placed into a 50 mL of 20 vol% TEOA solution. The visible-light irradiation was achieved from a 300 W xenon lamp with a UVCUT-420 nm filter. All tests are controlled at 15℃ by circulating condensate. Figure 7a presents the photocatalytic performance depending on the treatment time of KCl. The H_2 production rate of CN was 11.8 μmol/h. Their activity increases sharply with the heat treatment of KCl. Among all samples, KCN 2 presents the highest activity of 261.9 μmol/h, which is ≈22 times higher than that of CN. Subsequently, the activity decreases gradually over heat treatment time. In order to illustrate the universality of our proposed strategy to induce the formation of BIEF through thermodynamically feasible diffusion, we synthesized the CN and KCN obtained from different precursors (urea, cyanamide and dicyandiamide) in the same way. As shown in Figures S7-8, similar to the KCN obtained from melamine precursor, the color of other KCN samples is obviously deepened to yellow, and its structure also presents the structure of typical CCN. In addition, those KCN samples showed 4 to 7 times higher activity than the corresponding original CN (Inset of a). These examples fully demonstrate the universality of our strategy.

A large specific surface area is conducive to better contact between the photocatalyst and the reaction solution and the generation of more active sites. In order to exclude the effect of specific surface area change on the activity and better explain the relationship between KCl treatment time and activity, the H_2 production rate normalized by specific surface area was calculated. As shown in Figure 7b, their normalized activities also exhibit a trend of first increasing and then decreasing with the treatment time of KCl. KCN 2 shows the highest rate of 557.2 μmol/h/m^2, which is ≈34 times higher than CN (16.3 μmol/h/m^2). In addition, the change of photocatalytic performance is consistent with the BIEF strength shown in Figure 6f. These results fully demonstrate that the BIEF induced by the concentration gradient of K^+ ions promote the photocatalytic activity. Photocatalytic cycling experiments are used to illustrate the stability of the materials. As shown in Figure 7c, after five photocatalytic cycles, the activity only declines by 8.4%, which fully demonstrates the photostability of KCN 2. Figure 7d displays the apparent quantum efficiency (AQE) test. The AQE of KCN 2 can reaches 13.5% at 420 nm, which is ≈22 times higher than CN (≈0.6%). At 470 nm, its AQE is still as high as 2.4%, while trace H_2 can be detected for CN. This red-shift of the photoresponse wavelength is matched with the change of UV-Vis DRS spectra observed in Figure 2d. We compared the reported CCN to objectively evaluate the activity of our materials. In order to exclude the great difference in activity caused by different test conditions, such as test

temperature, light power, catalyst quality, concentration and volume of sacrificial agent, Pt loading, etc., the improvement multiple of H_2 production activity of CCN compared with that of corresponding CN was taken as the standard. As shown in Figure 7e, our H_2 production activity is 34 times higher than original CN, and is at a relatively good level in reported CCN.[17,24,27,31-39]

Surface photovoltage spectroscopy (SPS) and steady-state and transient-state photoluminescence (PL) characterizations are used to investigate the BIEF induced transport and separation of photogenerated carriers. As shown in Figure 8a, a positive surface photovoltage (SPV) response band in the range of 350-500 nm is observed, which can be attributed to the band to band transition. After the intercalation of K^+ ions in heptazine-based melon framework, the SPV signal of KCN samples is sharply enhanced due to the improved crystallinity. Above all, the stronger BIEF induced by the concentration gradient of K^+ ions leads to the higher SPV response of KCN 2 than that of KCN 4. Figure S9 shows the TEM images of the photo-deposited Pt nanoparticles on KCN 2 and KCN 4 surface. In contrast, the Pt nanoparticles are relatively dispersed on the surface of KCN 2, but agglomerated on KCN 4, further confirming the BIEF induced charge separation. Compared to a band-to-band emission peak at ≈454 nm, the PL peak gradually redshifts to 472 nm in KCN samples (Figure 8b), which is consistent with the narrowed bandgap. In addition, the PL and BIEF intensity presents a similar trend with first decrease and then increase, as the extension of KCl processing time. This may be due to the BIEF greatly promotes the dissociation of excitons, resulting in the decrease of PL intensity.[32,40] The strongest PL emission peak of KCN 4 sample can be attributed to the weak BIEF. Similarly, the fluorescence lifetime also presents a similar change with fluorescence intensity. As shown in Figure 8c, KCN 2 exhibits faster fluorescence decay with an average lifetime of 2.33 ns than CN (2.79 ns) and KCN 4 (2.75 ns). The concentration gradient of K^+ ions induced BIEF can be described as shown in Figure 8d. By controlling the diffusion of K^+ ions from the surface to bulk in CN, its concentration gradient in KCN samples was successfully constructed, resulting in the continuous change of energy band position from surface to bulk. Most of all, this continuous change of energy band position can generate a BIEF, which promotes the separation of photogenerated carriers and the transport from bulk to the surface.

3. Conclusions

In summary, the concentration gradient of K^+ ions were successfully constructed by controlling the diffusion of K^+ ions from the surface to bulk in CN. The BIEF induced by this concentration gradient, greatly promotes the separation of photogenerated carriers and the transport from bulk to the surface. The intercalation of K^+ ions in heptazine-based melon framework are confirmed by elemental analysis, XRD, NMR, XPS, etc., and its concentration gradient and induced BIEF are well illustrated by EDX, etched XPS, AFM and zeta potential tests. Besides, the effect of induced BIEF on photogenerated carriers separation are also fully investigated by SPS, Pt photo-deposition, and steady-state and transient-state PL characterizations. Its optimized visible-light activity for H_2 evolution is ≈34 times higher than CN. Most of all, we have developed a strategy to construct the ions concentration gradient through ions diffusion to

induce an BIEF, and finally achieve efficient carrier separation. The results presented herein provide an attractive strategy to construct efficient photocatalytic systems.

Declarations

Supporting Information

More TG, elemental analysis, ICP, XPS, SEM, TEM and BET results are shown in the supplementary information.

Acknowledgment

This work was jointly supported by the Natural Science Foundation of China (51874199, 22078200), and the Research Grants for Postdoctor in Shenzhen and Guangdong Basic and Applied Basic Research Foundation (2019A1515111021).

References

1. Wang, X. *et al.* A metal-free polymeric photocatalyst for hydrogen production from water under visible light. *Nat. Mater.* **8**, 76-80 (2009).
2. Kessler, F. *et al.* Functional carbon nitride materials-design strategies for electrochemical devices. *Nat. Rev. Mater.* **2**, 17030 (2017).
3. Cao, S., Low, J., Yu, J. & Jaroniec, M. Polymeric photocatalysts based on graphitic carbon nitride. *Adv. Mater.* **27**, 2150-2176 (2015).
4. Lin, L., Yu, Z. & Wang, X. Crystalline carbon nitride semiconductors for photocatalytic water splitting. *Angew. Chem. Int. Ed.* **58**, 6164-6175 (2019).
5. Wang, X., Ren, W., Cheng, J., Ou, H. & Titirici, M. Enhancing Visible-light Hydrogen Evolution Performance of Crystalline Carbon Nitride by Defect Engineering. *ChemSusChem* **12**, 3257-3262 (2019).
6. Chen, X., Shen, S., Guo, L. & Mao, S. Semiconductor-based Photocatalytic Hydrogen Generation. *Chem. Rev.* **110**, 6503-6570 (2010).
7. Hisatomi, T., Kubota, J. & Domen, K. Recent advances in semiconductors for photocatalytic and photoelectrochemical water splitting. *Chem. Soc. Rev.* **43**, 7520-7535 (2014).
8. Osterloh, F. E. Inorganic nanostructures for photoelectrochemical and photocatalytic water splitting. *Chem. Soc. Rev.* **42**, 2294-2320 (2013).
9. Zhang, Z., Zhu, Y., Chen, X., Zhang, H. & Wang, J. A Full-Spectrum Metal-Free Porphyrin Supramolecular Photocatalyst for Dual Functions of Highly Efficient Hydrogen and Oxygen Evolution. *Adv. Mater.* **31**, 1806626 (2019).
10. Li, J., Cai, L., Shang, J., Yu, Y. & Zhang, L. Giant Enhancement of Internal Electric Field Boosting Bulk Charge Separation for Photocatalysis. *Adv. Mater.* **28**, 4059-4064 (2016).

11. Li, J., Zhan, G., Yu, Y. & Zhang, L. Superior visible light hydrogen evolution of Janus bilayer junctions via atomic-level charge flow steering. *Nat. Commun.* **7**, 11480 (2016).
12. Huang, H. *et al.* Macroscopic Polarization Enhancement Promoting Photo- and Piezoelectric-Induced Charge Separation and Molecular Oxygen Activation. *Angew. Chem. Int. Ed.* **56**, 11860-11864 (2017).
13. Yu, Y. *et al.* Surface Engineering for Extremely Enhanced Charge Separation and Photocatalytic Hydrogen Evolution on g-C_3N_4. *Adv. Mater.* **30**, 1705060 (2018).
14. Luo, Z., Li, C., Liu, S., Wang, T. & Gong, J. Gradient doping of phosphorus in Fe_2O_3 nanoarray photoanodes for enhanced charge separation. *Chem. Sci.* **8**, 91-100 (2017).
15. Abdi, F. F. *et al.* Efficient solar water splitting by enhanced charge separation in a bismuth vanadate-silicon tandem photoelectrode. *Nat. Commun.* **4**, 2195 (2013).
16. An, L., Park, Y., Sohn, Y. & Onishi, H. Effect of Etching on Electron-Hole Recombination in Sr-Doped $NaTaO_3$ Photocatalysts. *J. Phys. Chem. C* **119**, 28440-28447 (2015).
17. Xu, Y. *et al.* K^+-induced crystallization of polymeric carbon nitride to boost its photocatalytic activity for H_2 evolution and hydrogenation of alkenes. *Appl. Catal. B-Environ.* **268**, 118457 (2020).
18. Xu, Y. *et al.* Solid salt confinement effect: An effective strategy to fabricate high crystalline polymer carbon nitride for enhanced photocatalytic hydrogen evolution. *Appl. Catal. B-Environ.* **246**, 349-355 (2019).
19. Zhang, G., Xu, Y., He, C., Zhang, P. & Mi, H. Oxygen-doped crystalline carbon nitride with greatly extended visible-light-responsive range for photocatalytic H_2 generation. *Appl. Catal. B-Environ.* **283**, 119636 (2021).
20. Zhang, J. *et al.* Co-monomer control of carbon nitride semiconductors to optimize hydrogen evolution with visible light. *Angew. Chem. Int. Ed.* **51**, 3183-3187 (2012).
21. Shalom, M., Inal, S., Fettkenhauer, C., Neher, D. & Antonietti, M. Improving carbon nitride photocatalysis by supramolecular preorganization of monomers. *J. Am. Chem. Soc.* **135**, 7118-7121 (2013).
22. Schwinghammer, K. *et al.* Triazine-based carbon nitrides for visible-light-driven hydrogen evolution. *Angew. Chem. Int. Ed.* **52**, 2435-2439 (2013).
23. Zhang, G., Zhang, J., Zhang, M. & Wang, X. Polycondensation of thiourea into carbon nitride semiconductors as visible light photocatalysts. *J. Mater. Chem.* **22**, 8083-8091 (2012).
24. Lin, L. *et al.* Crystalline carbon nitride semiconductors prepared at different temperatures for photocatalytic hydrogen production. *Appl. Catal. B-Environ.* **231**, 234-241 (2018).
25. Lotsch, B. V. *et al.* Unmasking Melon by a Complementary Approach Employing Electron Diffraction, Solid-State NMR Spectroscopy, and Theoretical Calculations-Structural Characterization of a Carbon Nitride Polymer. *Chem. Eur. J.* **13**, 4969-4980 (2007).
26. Holst, J. & Gillan, E. From triazines to heptazines: deciphering the local structure of amorphous nitrogen-rich carbon nitride materials. *J. Am. Chem. Soc.* **130**, 7373-7379 (2008).

27. Lin, L., Ou, H., Zhang, Y. & Wang, X. Tri-s-triazine-Based Crystalline Graphitic Carbon Nitrides for Highly Efficient Hydrogen Evolution Photocatalysis. *ACS Catal.* **6**, 3921-3931 (2016).
28. Ihs, A., Uvdal, K. & Liedberg, B. Infrared and photoelectron spectroscopic studies of ethyl and octyl xanthate ions adsorbed on metallic and sulfidized gold surfaces. *Langmuir* **9**, 733-739 (1993).
29. Shaw, D. J. Introduction to Colloid and Surface Chemistry. 298-306 (Butterworth-Heinemann, 1992).
30. Guo, Y., Shi, W., Zhu, Y., Xu, Y. & Cui, F. Enhanced photoactivity and oxidizing ability simultaneously via internal electric field and valence band position by crystal structure of bismuth oxyiodide. *Appl. Catal. B-Environ.* **262**, 118262 (2020).
31. Lin, L. *et al.* Photocatalytic overall water splitting by conjugated semiconductors with crystalline poly(triazine imide) frameworks. *Chem. Sci.* **8**, 5506-5511 (2017).
32. Zhang, G. *et al.* Optimizing Optical Absorption, Exciton Dissociation, and Charge Transfer of a Polymeric Carbon Nitride with Ultrahigh Solar Hydrogen Production Activity. *Angew. Chem. Int. Ed.* **56**, 13445-13449 (2017).
33. Chen, Z. *et al.* "The Easier the Better" Preparation of Efficient Photocatalysts-Metastable Poly(heptazine imide) Salts. *Adv. Mater.* **29**, 1700555 (2017).
34. Zhang, G. *et al.* Electron Deficient Monomers that Optimize Nucleation and Enhance the Photocatalytic Redox Activity of Carbon Nitrides. *Angew. Chem. Int. Ed.* **58**, 14950-14954 (2019).
35. Zeng, Z., Yu, H., Quan, X., Chen, S. & Zhang, S. Structuring phase junction between tri-s-triazine and triazine crystalline C_3N_4 for efficient photocatalytic hydrogen evolution. *Appl. Catal. B-Environ.* **227**, 153-160 (2018).
36. Schwinghammer, K. *et al.* Crystalline Carbon Nitride Nanosheets for Improved Visible-Light Hydrogen Evolution. *J. Am. Chem. Soc.* **136**, 1730-1733 (2014).
37. Dontsova, D. *et al.* Triazoles: A New Class of Precursors for the Synthesis of Negatively Charged Carbon Nitride Derivatives. *Chem. Mater.* **27**, 5170-5179 (2015).
38. Wu, M., Yan, J. M., Tang, X. N., Zhao, M. & Jiang, Q. Synthesis of Potassium-Modified Graphitic Carbon Nitride with High Photocatalytic Activity for Hydrogen Evolution. *Chemsuschem* **7**, 2654-2658 (2014).
39. Qiu, C. *et al.* Highly Crystalline K-Intercalated Polymeric Carbon Nitride for Visible-Light Photocatalytic Alkenes and Alkynes Deuterations. *Adv. Sci.* **6**, 1801403 (2019).
40. Wang, H. *et al.* Boosting Hot-Electron Generation: Exciton Dissociation at the Order-Disorder Interfaces in Polymeric Photocatalysts. *J. Am. Chem. Soc.* **139**, 2468-2473 (2017).

Figures

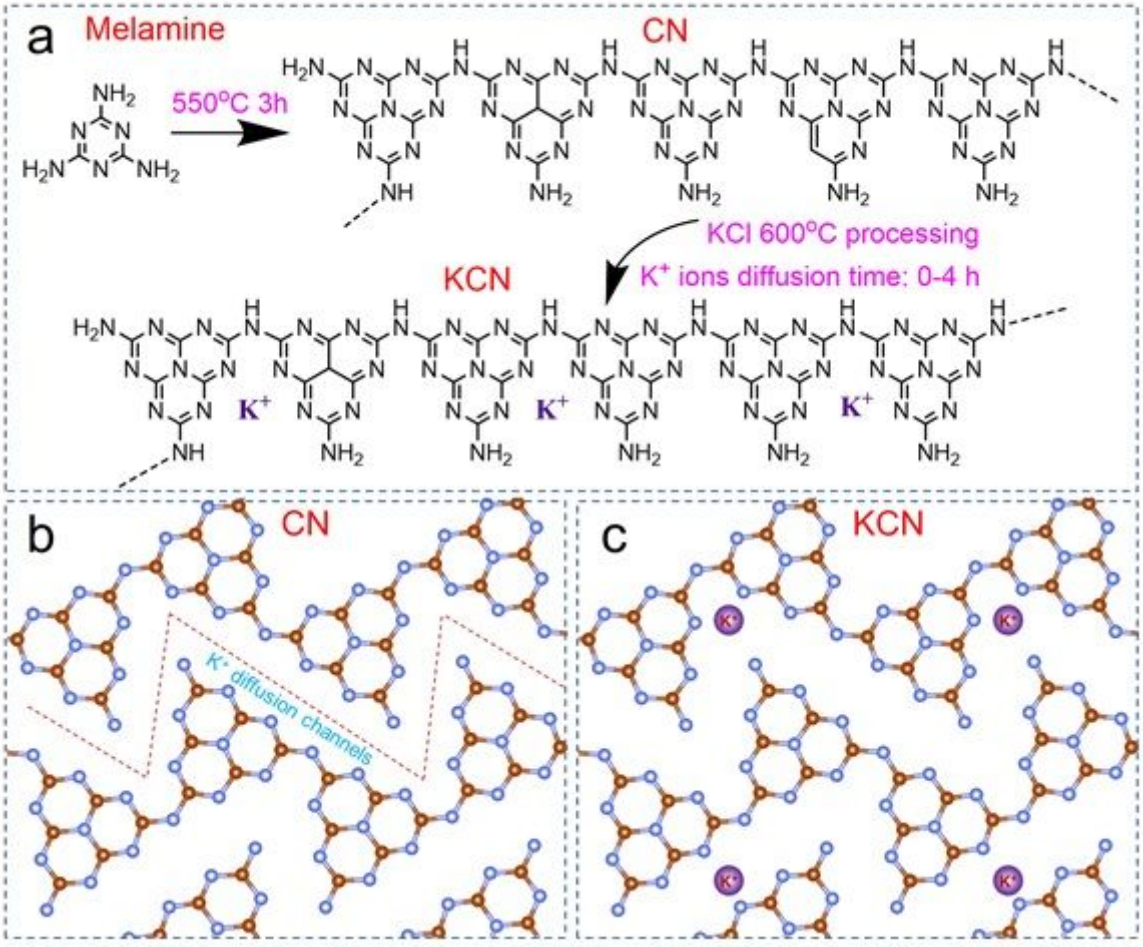

Figure 1

Possible synthetic processes for KCN samples (a). The proposed molecular structure diagram of CN (b) and KCN (c). The atoms of C, N and K are in brown, light blue and purple, respectively.

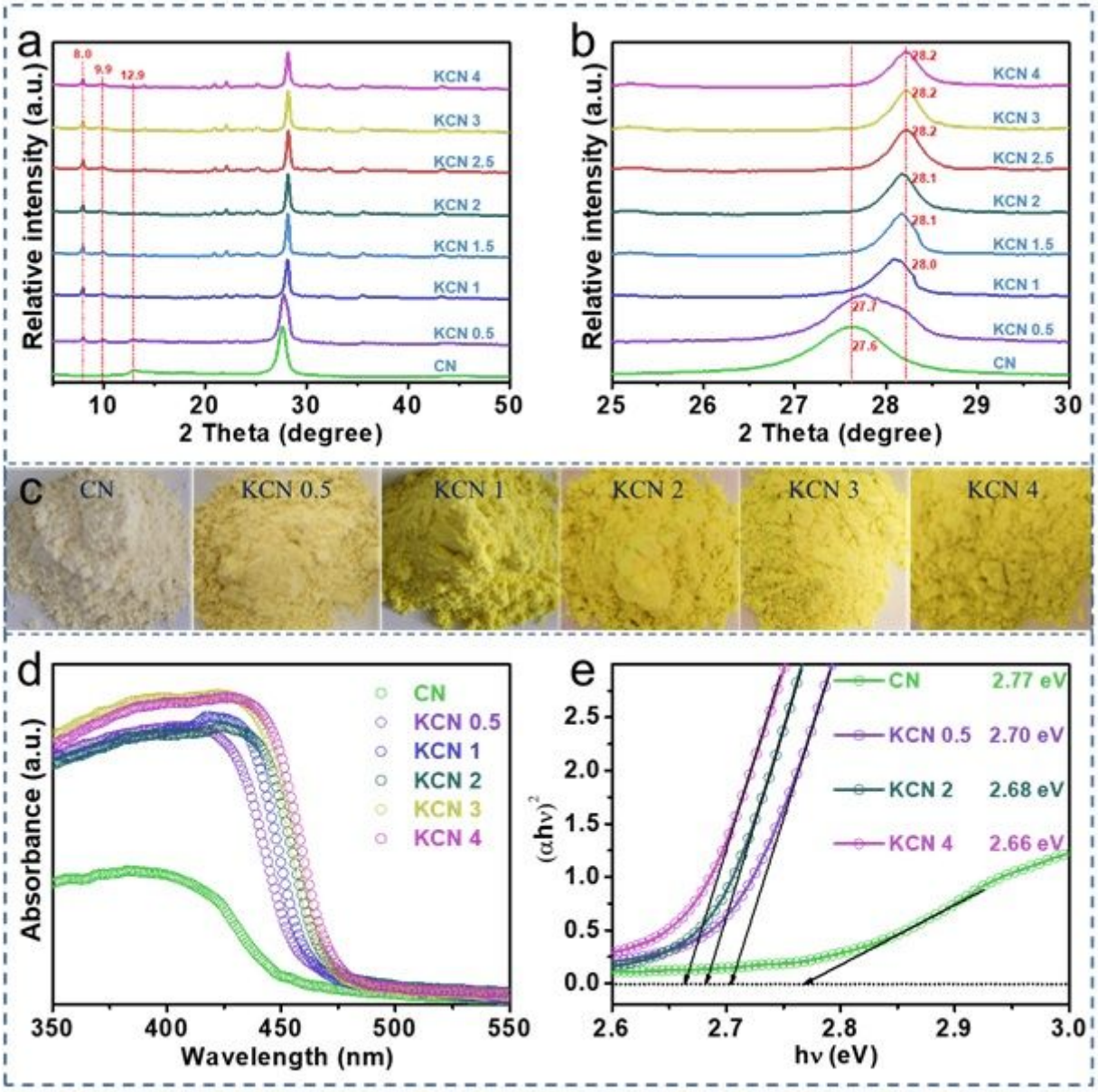

Figure 2

The XRD patterns (a-b), optical images (c), UV-Vis DRS spectra (d) and Tauc plots of the transformed Kubelka-Munk function vs. the energy (e) of CN and KCN x (x = 0.5-4).

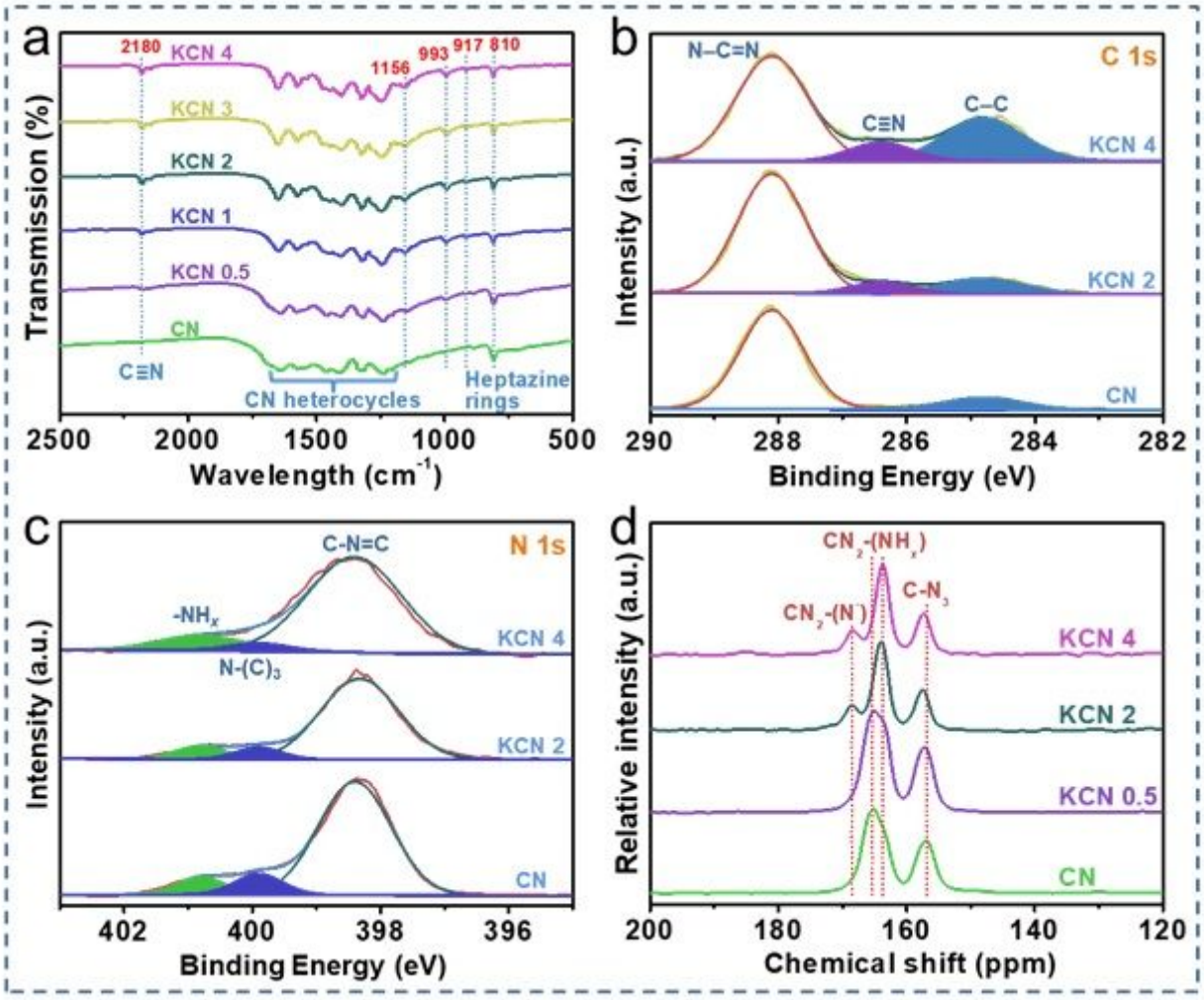

Figure 3

The FTIR spectra (a), high-resolution XPS spectra (b-c) and solid-state CP/MAS 13C NMR spectra (d) of CN and KCN x (x = 0.5-4).

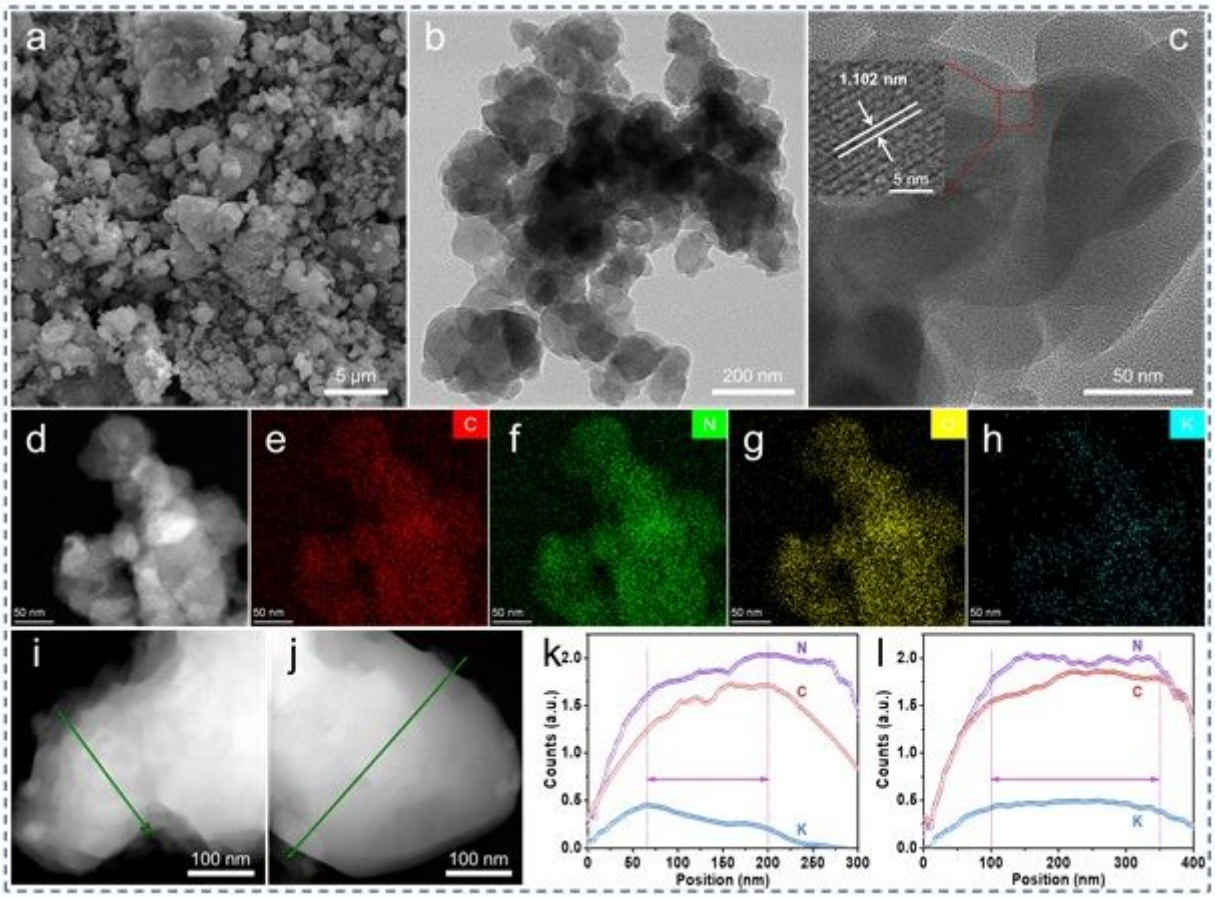

Figure 4

The SEM (a) and TEM images (b-c) of KCN 2. Inset in (c) is the HR-TEM image. HAADF-STEM image (d) and the corresponding elemental mappings of C, N, O and K distribution (e-h) in KCN 2. HAADF-STEM images (i-j) and the EDX lines from a single nanoparticle (k-l) in KCN 2 and KCN 4, respectively.

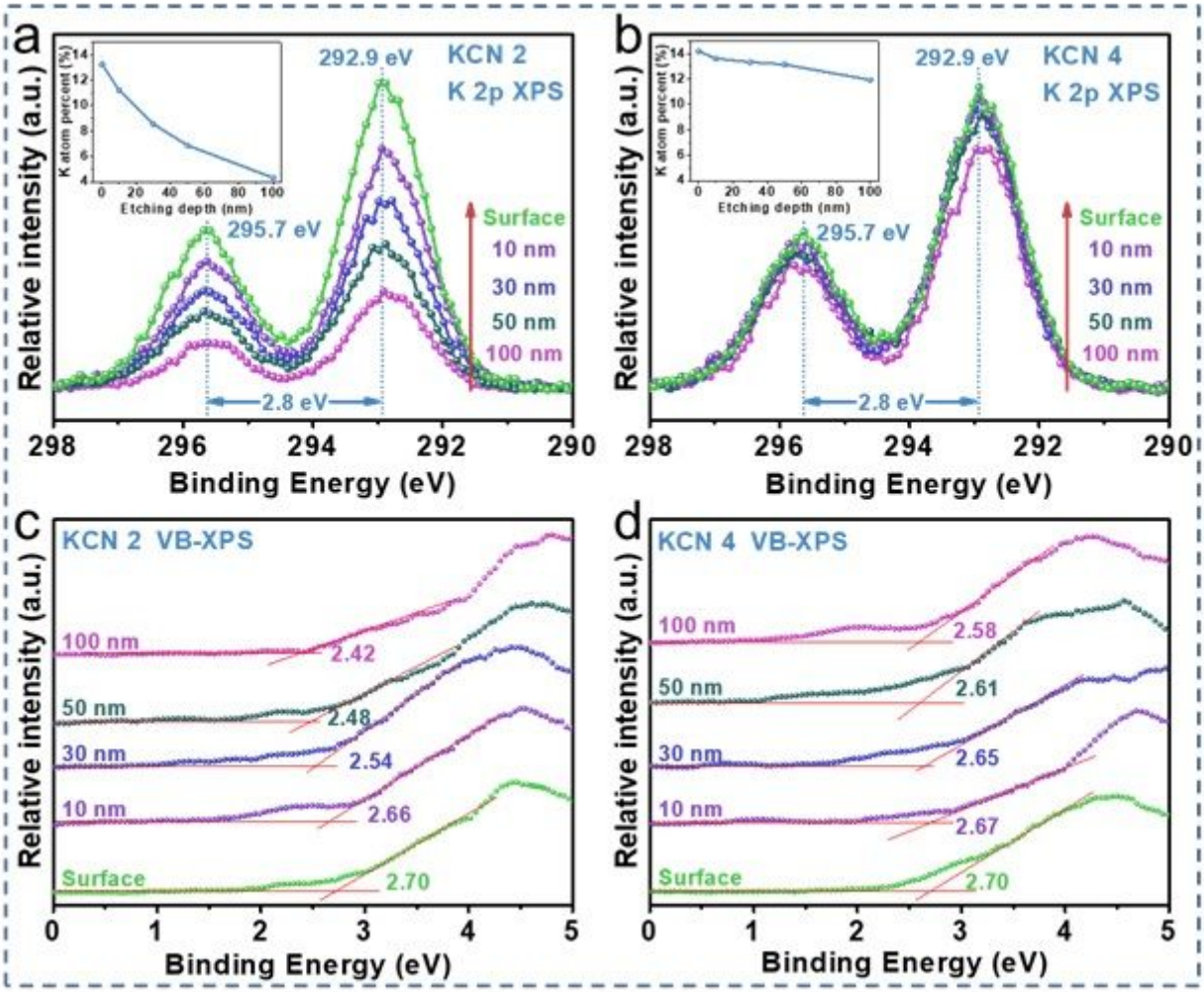

Figure 5

Argon ion etched K 2p XPS (a-b) and VB-XPS (c-d) at different depths (0-100 nm) in KCN 2 and KCN 4.

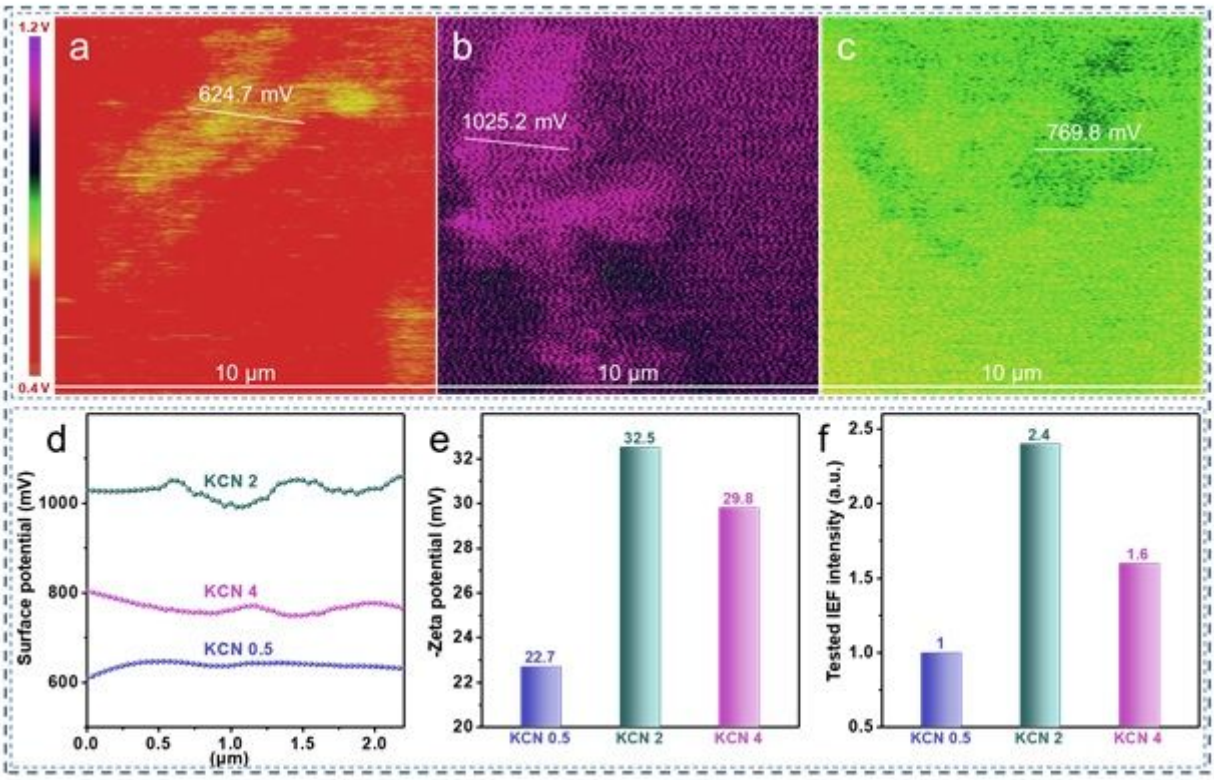

Figure 6

AFM images at the surface potential mode for KCN 0.5 (a), KCN 2 (b) and KCN 4 (c). Surface potential profiles (d) along the lines in Figures 6a-c, zeta potential value (e) and tested BIEF (f) (assuming the intensity of KCN 0.5 to be “1”) for KCN 0.5, KCN 2 and KCN 4.

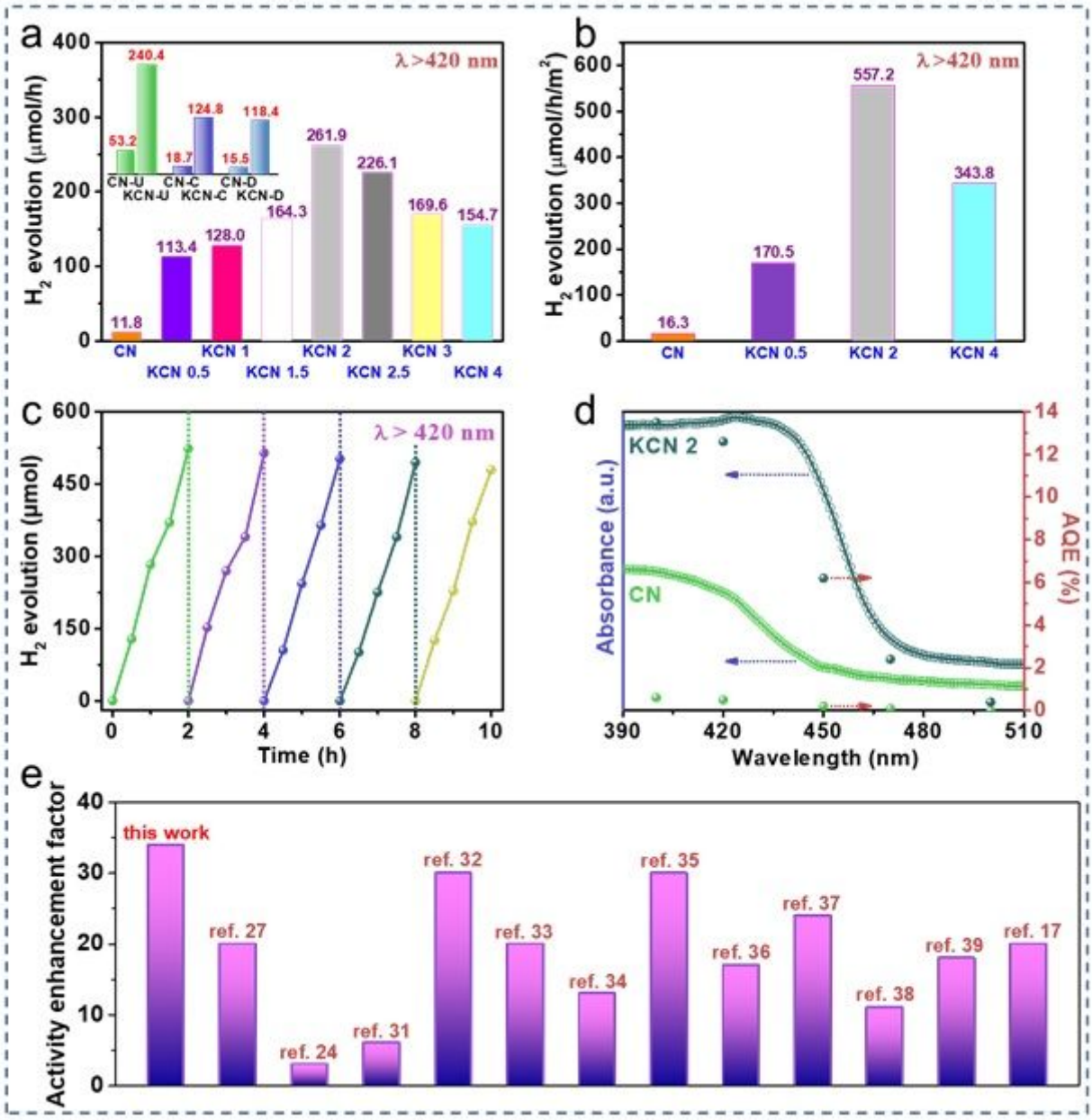

Figure 7

The H2 production rate (a) and normalized rate of specific surface area (b) of CN and KCN x (x = 0.5-4) under λ > 420 irradiations. Inset of a is the H2 production rate of CN and KCN obtained from different precursors (urea, cyanamide and dicyandiamide) under λ > 420 irradiations. The recycling measurements of the H2 production over KCN 2 (c). Wavelength-dependent apparent quantum yield of CN and KCN 2 under monochromatic light irradiation (d). Comparison of activity enhancement factor with the reported CCN photocatalysts compared to the corresponding CN (e).

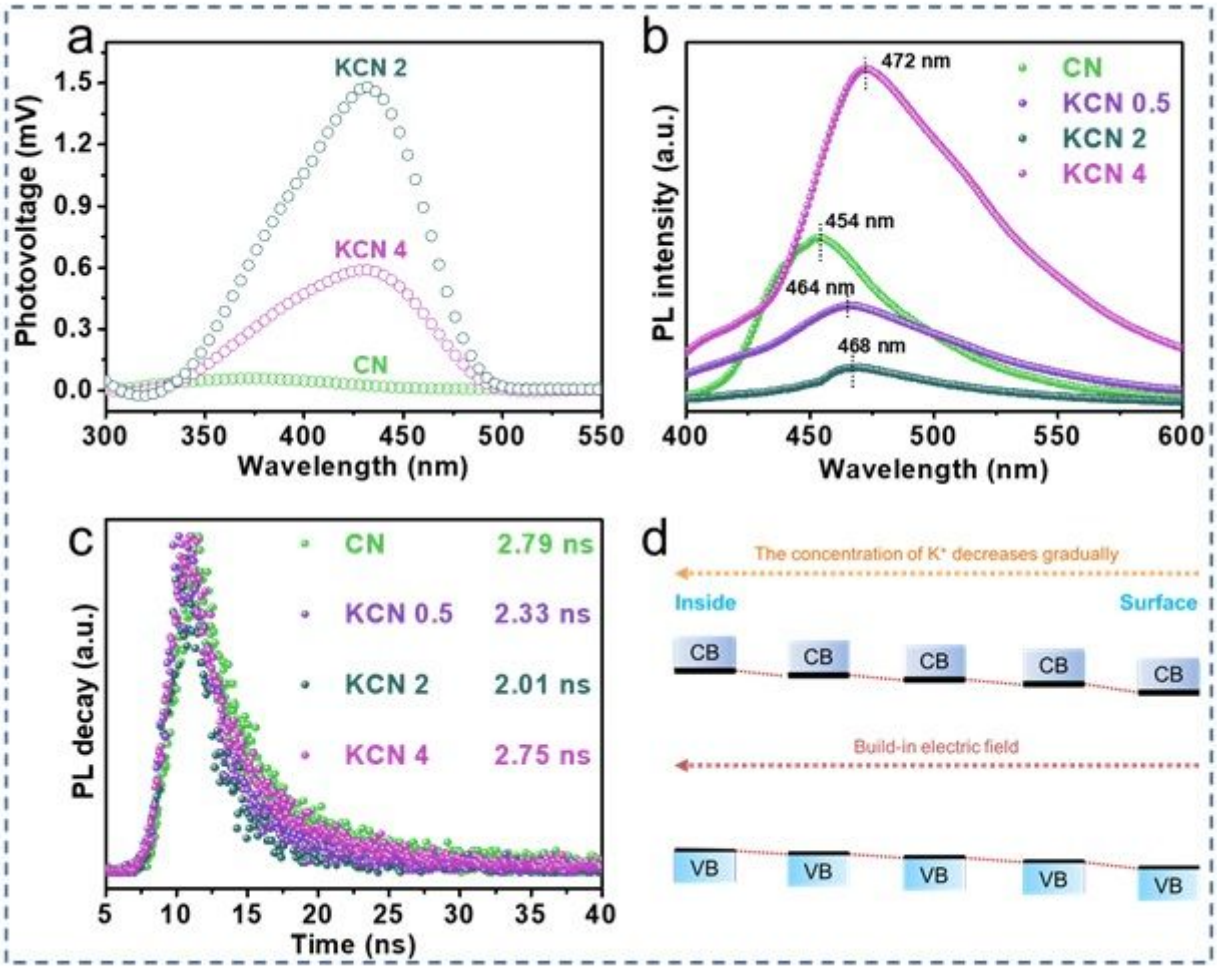

Figure 8

The SPS (a), steady-state (b) and transient-state PL (c) of CN and KCN x (x = 0.5-4). Schematic diagram of a BIEF induced by a K+ concentration gradient (d).

Supplementary Files

This is a list of supplementary files associated with this preprint. Click to download.

- SupportingInformation.docx